

# Cluster time measurement with CEPC calorimeter

Yuzhi Che<sup>1,2</sup>, Vincent Boudry<sup>3</sup>, Henri Videau<sup>3</sup>, Muchen He<sup>1</sup>, Manqi Ruan<sup>a,1</sup>

<sup>1</sup>Institute of High Energy Physics, Chinese Academy of Sciences, Beijing 100049, China

<sup>2</sup>University of Chinese Academy of Sciences, 19A Yuquan Road, Beijing 100049, China

<sup>3</sup>LLR, Ecole Polytechnique, Palaiseau, France

Received: date / Accepted: date

**Abstract** We have developed an algorithm dedicated to timing reconstruction in highly granular calorimeters(HGC). The performance of this algorithm is evaluated on an electromagnetic calorimeter (ECAL) with geometries comparable to the electromagnetic compartment (CE-E) of the CMS endcap calorimeter upgrade at HL-LHC and conceptual Particle Flow oriented ECAL's for future Higgs factories. The time response of individual channel is parameterized according to the CMS experimental result [1]. The particle Time-of-Flight (ToF) can be measured with a resolution of  $5 \sim 20$  ps for electromagnetic (EM) showers and  $80 \sim 160$  ps for hadronic showers above 1 GeV. The presented algorithm provides comparable reconstruction with the  $E_{\text{hit}}^2$  weighting strategy and can significantly improve the time resolution compared to a simple averaging of the fast component of the time spectrum. The effects of three detector configurations are also quantified in this study. ToF resolution depends linearly on the timing resolution of a single silicon sensor and improves statistically with increasing incident particle energy. The timing layers at depth of  $6 \sim 9$  radiation lengths provide higher timing performance for EM showers. A clustering algorithm that vetoes isolated hits improves ToF resolution.

**Keywords** Time of Flight · High Granularity Calorimeter

## 1 Introduction

Precise Time-of-Flight (ToF) reconstruction is important for experiments in particle physics at the high energy frontier. As the world's most powerful particle

accelerator, the Large Hadron Collider (LHC) is expected to deliver proton-proton collisions with an integrated luminosity of  $300 \text{ fb}^{-1}$  by the end of 2023. From 2026 to about 2030, this machine will be upgraded into the High Luminosity configuration (HL-LHC) [2] and collect  $3000 \text{ fb}^{-1}$  more data. With a tenfold increase in luminosity, the corresponding number of collisions per bunch crossing (a.k.a. pile-up) is expected to be  $140 \sim 200$ ,  $5 \sim 7$  times the value of the LHC. The event selection and characterisation at the HL-LHC will face the increasing difficulty of assigning the detector signals to the correct interaction. Since the typical time spread of pile-up events is at the hundred picosecond level, a ToF measurement with a resolution of about  $20 \sim 30$  ps can significantly mitigate the effect of pile-up [3–7].

For future electron-positron colliders, the  $e^-e^+$  Higgs factories are identified as the highest-priority next collider by the European Strategy statement [8]. As one of the collider concepts, the circular  $e^-e^+$  collider can also operate at a center-of-mass energy of 91.2 GeV for a Z factory with high luminosity, providing a valuable flavor physics opportunity. Particle identification (PID) is critical for flavor physics measurements. A common method for separating  $K/\pi/p$  is to measure the ToF and  $dE/dx$  of the particles. The  $K/\pi$  and  $K/p$  separation power provided by  $dE/dx$  decreases sharply as the particle momentum approaches 1 GeV and 2 GeV. Therefore, the ToF plays an essential role in compensating for the lack of PID performance provided by  $dE/dx$ . For instance, a ToF precision better than 50 ps makes significant PID improvement at the CEPC [9].

The concept of high granularity calorimetry concept is widely applied in the upgrade detectors for the HL-LHC and will also be used in the detectors of future electron-positron colliders. Multiple prototypes have been constructed by the CALICE, CMS, and LHCb collabo-

<sup>a</sup>e-mail: ruanmq@ihep.ac.cn

rations and have shown promising performance in beam tests [4, 10, 11]. This concept proposes extremely high spatial segmentation. For instance, the baseline ECAL of the CEPC has about three active cells per cubic centimeter. Its longitudinal thickness of 24 radiation lengths ( $X_0$ ) is divided into 30 sampling layers. Its transverse cell size is only  $1 \times 1 \text{ cm}^2$ . Such an ECAL can generate hundreds of hits, i.e., cells with a signal above a readout threshold, for a 10 GeV photon or pion, as shown in Fig. 1. The Particle Flow Algorithms (PFA) make full use of the HGC. They combine the signals from the sub-detectors into a list of reconstructed 'particle flow objects', which ideally have a one-to-one correspondence with the incident particles. The PFA includes a clustering algorithm and a matching algorithm. The first one groups the calorimeter hits into clusters according to the hit position, and the second module matches the clusters to the trajectory in the tracker.

Further, HGC can be enhanced with the timing measurement of individual cells. Depending on the applications, the precision can range from ns to 10's ps. Several factors limit the precision. One natural factor is the signal collection spread, typically the cell size divided by the speed of light. Signal noise and clock jitter further degrade the performances at low and high amplitudes, respectively [1, 12, 13]. This timing readout capability makes it possible to measure a particle ToF by appropriately combining the cell information. Averaging the times measured by multiple cells with charge-weighting, the current silicon timing layers have shown time resolution higher than 25 ps [13–15]. Moreover, measurement of the shower inner timing spectrum is hopeful of extending the clustering of the PFA.

This work focus on the timing measurement using high-granularity ECAL's. After a brief introduction of the involved detector configuration and simulation software (Sec. 2), we analyse the shower true time spectrum and the effect of intrinsic hit time resolution (Sec. 3). In Sec. 4, we propose a time reconstruction algorithm based on the quantile of the shower time spectrum. We conclude that ToF resolutions of  $5 \sim 20$  ps for EM showers and  $80 \sim 160$  ps for hadronic showers are achievable in the CEPC ECAL. In section 5, we explore the dependence of time resolution on: (a) the intrinsic time resolution of each individual channel and (b) the number of timing readout layers. The expected timing performance of the CMS CE-E is extrapolated from the result of the CEPC ECAL. It is affected by the clustering algorithm, which is studied in Sec. 6. The next section gives a brief summary. The algorithm proposed here is compared with an alternative timing strategy in Appendix A.

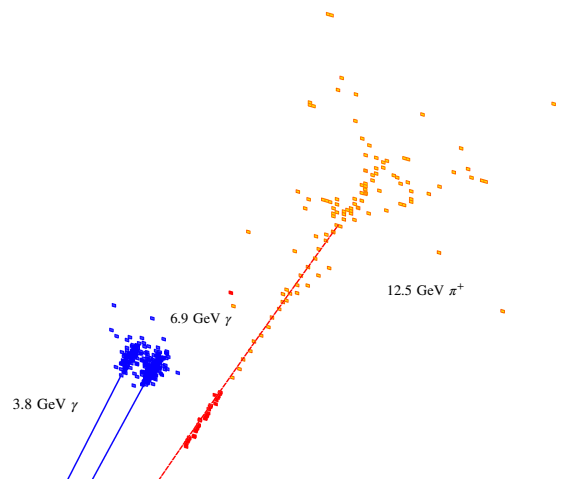


**Fig. 1** The event display of two photons and one charged pion, generated from a hadronic  $\tau$  decay. The blue hits around the blue solid lines are the ECAL hits of a 3.8 GeV photon shower and a 6.9 GeV photon shower. The red hits around the red dashed line are the ECAL hits belonging to a 12.5 GeV  $\pi^+$  shower, while the orange hits are the HCAL hits of the same  $\pi^+$  shower. The size of these cells is  $1 \times 1 \text{ cm}$ .

## 2 Detector and software

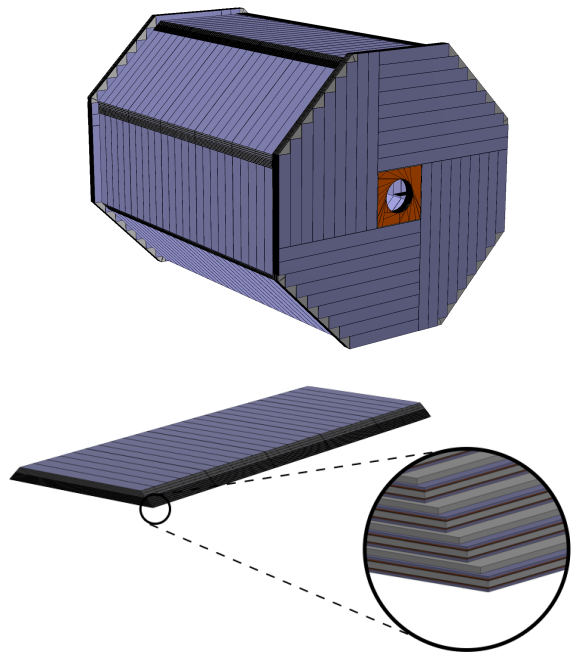


**Fig. 2** Geometry of the CEPC ECAL (top) and a display of one ECAL stave [16] (bottom).

This study is based on the full simulation with the geometry of the CEPC baseline ECAL. The ECAL geometry has been optimized based on the PFA require-

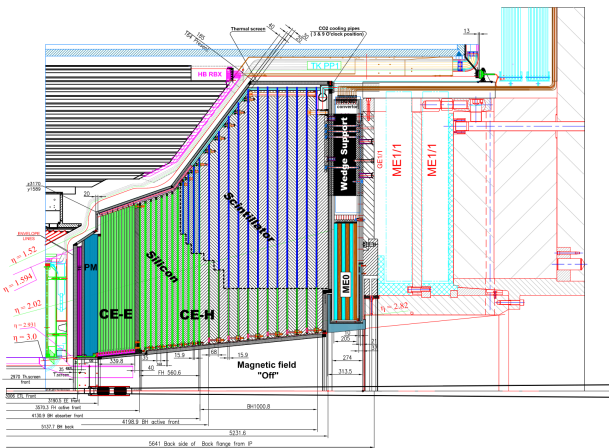


**Fig. 3** Longitudinal cross-section of the upper half of the CMS endcap calorimeter [4].

ment. This calorimeter features an eight-stave barrel and two octagonal endcap sections (Fig. 2). The inner radius of the barrel is 1847 mm, and the distance between the Interaction Point (IP) and the front face of the ECAL endcap is 2450 mm. In the radial direction, the ECAL is segmented into 30 sampling layers, each consisting of a tungsten absorber and an active layer. The thickness of the tungsten plates in the first 20 layers is 0.6 radiation lengths ( $X_0$ ), and double in the last ten layers. Each active layer is equipped with square matrices of highly resistive silicon diodes, segmented in cells of  $10 \times 10 \text{ mm}^2$  and a thickness of 0.5 mm. The CEPC ECAL includes around  $2 \times 10^7$  channels.

The HGC concept is also applied to upgrading the CMS endcap calorimeters, now in construction, whose geometry is shown in Fig. 3. It comprises an electromagnetic compartment (CE-E) and a hadronic calorimeter (CE-H). The CE-E is a sampling calorimeter equipped with silicon sensors and tungsten absorbers. Along the direction of the beam pipe, the CE-E is installed in the range from  $|z| = 3.19 \text{ m}$  to  $3.53 \text{ m}$ , for an IP at  $z = 0$ . In the cross-section perpendicular to the beam pipe, CE-E has a disk-like shape with an inner and outer radius of 0.32 m and 1.68 m at the front face. The total longitudinal thickness of  $27.7 X_0$  is divided into 26 sampling layers [17]. The radiation fluence increases with the increasing pseudorapidity ( $\eta$ ). In order to maintain the performance after the integrated luminosity of  $3000 \text{ fb}^{-1}$ , the disk-like CE-E is divided into three rings corresponding to  $r = 35 \sim 70 \text{ mm}$ ,  $70 \sim 100 \text{ mm}$  and  $100 \sim 180 \text{ mm}$ . From the inside out, the radiation fluence decreases. Three types of silicon sensors with deployment thickness of  $120 \mu\text{m} \times 0.52 \text{ cm}^2$ ,  $200 \mu\text{m} \times 0.52 \text{ cm}^2$ ,  $300 \mu\text{m} \times 1.18 \text{ cm}^2$  are equipped in these three regions. The total number of channels is

$3.916 \times 10^6$ . The granularity information of the CE-E and the CEPC ECAL is shown in Tab. 1. In this paper, we extrapolate the evaluated timing performance in the CEPC ECAL to that in the CMS CE-E.

To quantify the ToF performance of the CEPC ECAL, we simulate ECAL showers resulting from single  $\gamma$ ,  $e^-$ ,  $\pi^+$ ,  $K^+$  and p using a full simulation package based on GEANT4 [18]. For reference, we also simulated the energy deposition of muons, which are close to minimum ionization particles (MIP). The momentum of the created particles is at a single value or uniformly distributed in a range from 0 to 30 GeV. The particle originates from a point 193 mm from the IP<sup>1</sup> and is shot perpendicular to the ECAL surface. The magnetic field is turned off so that charged particles propagate to ECAL along straight lines, and the redundant discussion about trajectory correction is simplified. The statistic of the involved samples is listed in Tab. 2.

**Table 1** Geometry, granularity and active material of the CMS HGCAL(CE-E) [4, 17] and the CEPC ECAL [16].

	CMS HGCAL	CEPC ECAL
Sensitive material	Silicon	Silicon
Layers number	26	30
Total thickness	$27.7 X_0$	$24 X_0$
Cell size	$\sim 0.5/1.1 \text{ cm}^2$	$1 \text{ cm}^2$
Cell shape	hexagon	square

**Table 2** Statistics of the simulated single particle samples. Six samples were generated with uniformly distributed incident momentum, while three samples with single incident momentum.

Particle	$\gamma$	$e^-$	$\mu^-$	$\pi^+$	$K^+$	p
Energy [GeV]	0 – 30	0 – 30	0 – 30	0 – 30	0 – 30	0 – 30
Event Num.	$3 \times 10^4$	$3 \times 10^4$	$3 \times 10^4$	$3.6 \times 10^4$	$3.6 \times 10^4$	$3.6 \times 10^4$
Energy [GeV]	10	-	10	10	-	-
Event Num.	$5 \times 10^3$	-	$5 \times 10^3$	$5 \times 10^3$	-	-

### 3 Shower energy-time spectrum

We first investigate the distribution of the hit time at the truth level. Secondly, we implement a time digitization process according to the CMS beam test result on the intrinsic time resolution of the single silicon sensor [1]. We discuss the digitized time spectrum pattern, which is supposed to be fully accessible at the CEPC ECAL.

<sup>1</sup>To avoid early interactions

**Fig. 4** The distribution of the true projected hit time in the range of  $< 6$  ps in the 10 GeV  $\gamma$ ,  $\pi^+$  and  $\mu^-$  samples (left) and the corresponding cumulative distribution in the time range of  $0 \sim 1 \mu\text{s}$  (right). The dashed lines in the left plot are the expected time when the incident particles reach the front of the ECAL. In the right plot, the solid black line corresponds to the boundary (6 ps) of the left plot. To show the complete cumulative distribution, the x-axis of the right plot uses a symmetrical logarithmic scale, which is linear in the range of  $[-2, 2]$  ps and logarithmic in the other region. The total number of all the hits earlier than  $1 \mu\text{s}$  is normalized to unity in these two plots, which means the integral of the distribution in the left plot equals to the corresponding value in the right cumulative distribution.

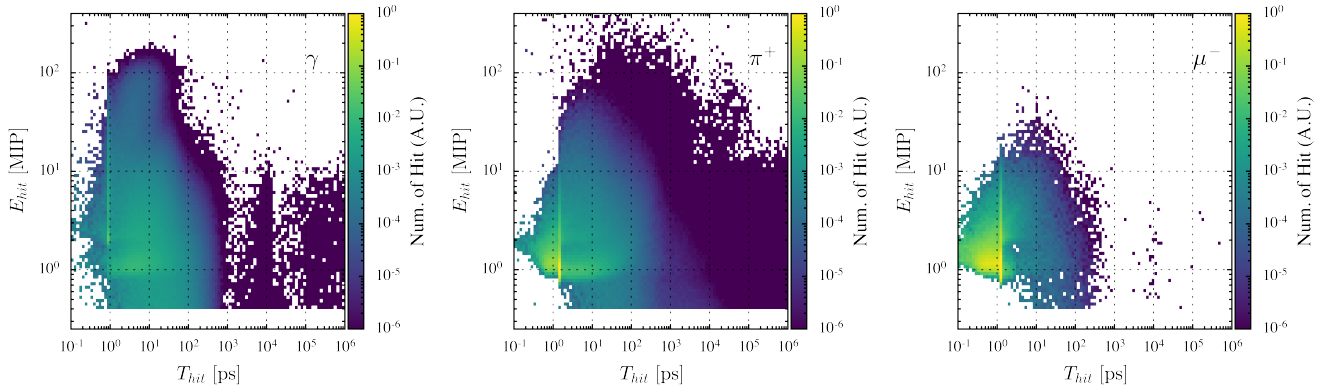
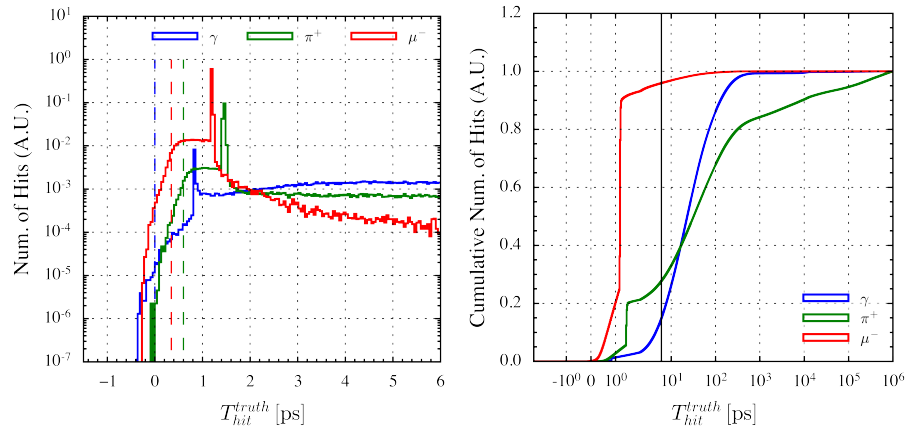


**Fig. 5** The two-dimensional probability density distribution of the hits projected time and energy in 10 GeV  $\gamma$  (left),  $\pi^+$  (middle) and  $\mu^-$  (right) samples. The total number of all the hits earlier than  $1 \mu\text{s}$  is normalized to unity.

The true information of each hit is extracted from the steps and tracks in the cell generated by Geant4. The zero time is fixed to when the particle is created. The energy of the hits given in GeV is normalized in units of MIPs (0.147 MeV), where a MIP is defined as the most probable value of the energy deposition in a silicon sensor by a 10 GeV muon hitting perpendicularly. Only the hits with energy higher than 0.05 MeV or about  $1/3$  MIPs are considered in our analysis. Hits occurring after  $1 \mu\text{s}$  are ignored, this time threshold is larger than the time spread of pile-up events at the HL-LHC and the time spacing of the bunch crosses at the CEPC. To perfectly reflect the behavior of the timing electronics, a good definition of the true times of cell hits is to select the earliest time above an energy threshold. However, the energy threshold depends strongly on the specific discriminator in the electronic. In this study, true hit times are defined as the time of

the most energetic step in the cell. This approximation differs only slightly from the previous definition because the cases of multiple energetic but well-separated depositions in time are rare.

Fig. 4 shows the true hit time spectrum of 10 GeV photons, charged pions, and muons, as well as the expected ToFs of these three types of particles. In these plots, the time is redefined as the projected time,

$$T = t - L/c \quad (1)$$

where  $t$  denotes the raw hit times,  $L$  denotes the distance between the IP and the center of the hit. Since the magnetic field is set to zero, this subtraction approximately normalizes the propagation time from the IP to the ECAL hit. Each distribution contains a fast component from 0 to 2 ps, followed by a slow tail extending beyond one ns. During the simulation, there are a large amount of hits including only one step and paus-



ing a peak in the fast component. The hits with multiple steps contribute to the platform before the peak. Moreover, the finite granularity of the ECAL causes an error in  $L$ . Consequently, there is a small fraction of shower hits whose projected time is before zero.

The three plots in Fig. 5 show the correlation between the hit time and energy for showers produced by 10 GeV  $\gamma$ 's,  $\pi^+$ 's and  $\mu^-$ 's. A large fraction of hits has energy lower than 5 MIPs. The energy deposition corresponding to one and two MIPs are visible. The shadows around 10 ns for photons arises from the back-scattering hits in the opposite side of the ECAL. In addition, the photon and pion showers include an extremely slow component later than 100 ps with a fraction of 15% and 30%, respectively, which may constitute noise in the next physics event. More importantly for the timing of the showers, the energetic hits tend to occur in the fast component of the showers, especially in the EM showers. The energy of the hits with projected time from 0 to 100 ps ranges from several MIPs to around 100 MIPs in the first plot of Fig. 5.

To mimic the effect of the detector and its readout electronics, we implement a digitization process based on the CMS beam test results on the time response of the thin planar silicon diodes [1]. In the CMS report, the intrinsic hit time resolution has been measured by the independent returns of two parallel sensors, as

$$\frac{\sigma(t_1 - t_2)}{\sqrt{2}} = \frac{A}{\sqrt{2}S_{\text{eff}}} \oplus C, \quad (2)$$

where  $S_{\text{eff}} = S_1 S_2 / \sqrt{S_1^2 + S_2^2}$  and  $S_1, S_2$  denotes the signal strength of the two sensors. For the sensors with depletion thickness of 211  $\mu\text{m}$ , the coefficients  $A$  and  $C$  are respectively 380 ps  $\cdot$  MIP and 10ps. Accordingly, we smeared the simulated true time of each hit with a Gaussian response function. The width of the response function equals the intrinsic hit time resolution parameterized as  $\sigma = \frac{A}{E} \oplus C$ ,  $A = 380$  ps  $\cdot$  MIP and  $C = 10$ ps.  $E$  denotes the energy deposition in MIP units and is equivalent to  $\sqrt{2}S_{\text{eff}}$ . The resulting time resolution as a function of hit energy is shown in Fig. 6. When the hit energy is higher than 100 MIPs, the intrinsic hit time resolution saturates at 10 ps. However, a large amount of hits in the showers have only an energy of several MIPs, for which the intrinsic hit time resolution is worse than 100 ps.

Fig. 7 shows the projected time spectrum of showers after time digitization. The fast component, which occurs before the first ten ps on the truth level (Fig. 4), is smeared into the  $-0.5$  to  $0.5$  ns region, where the digitization uncertainty dominates the shape. The shape of the fast component distribution is a highly

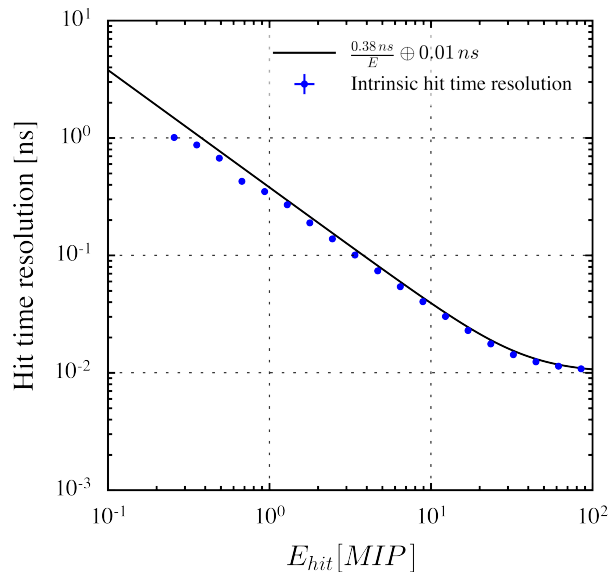


**Fig. 6** The intrinsic hit time resolution as a function of the energy deposition in the silicon sensors. The black solid line is the model of CMS measurement [1] and the blue dots are the result of the digitization in the 10 GeV  $\mu^-$  samples.

non-Gaussian peak, as it is a combination of various resolutions. The slow component at the truth level is also retained after digitization, and its fraction differs according to the shower types. The fraction of the hits with projected time above one ns is almost zero in photon and muon but about 20% in pion showers.

#### 4 A ToF reconstruction algorithm

Considering the non-Gaussian distribution and the later tail of the digitized shower time, a blind average of the hits brings many biases. We propose a universal shower time reconstruction algorithm based on a given quantile of the projected hit times.

Starting with the collection of all digitized hit times of the cluster, we sort the times in ascending order and use the value of the  $(R \cdot N_{\text{hits}})$ -th as a result, where  $R$  is an ad hoc ratio and  $N_{\text{hits}}$  is the number of the shower hits. When  $R < 0.5$ , the result corresponds to the median of the fastest  $2R \cdot N_{\text{hits}}$  hit time.

The single parameter  $R$  should be optimized for a reasonable time reconstruction. In the following section, we qualify the algorithm's performance in bias and resolution and discuss their behavior under variations of  $R$ .

##### 4.1 Performance for single particle showers

The input of the algorithm is the projected times of the hits in the shower. A dedicated clustering algorithm is

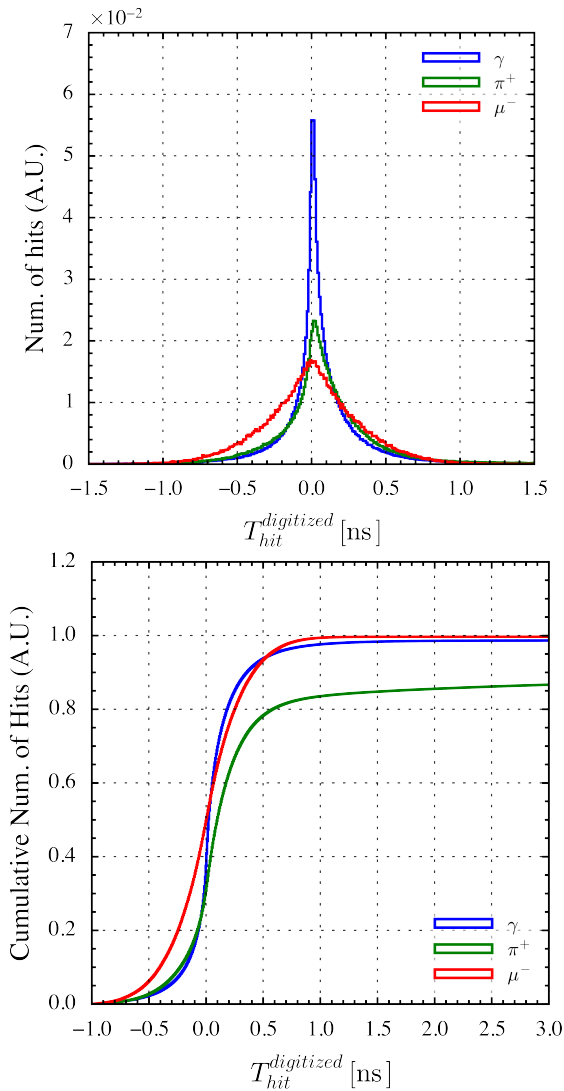


**Fig. 7** The digitized hit time distribution in range of  $-1 \sim 1.5$  ns of 10 GeV  $\gamma$ ,  $\pi^+$  and  $\mu^-$  (top) and the cumulative distribution in the time range of  $-1 \sim 3$  ns (bottom), where the total number of all the hits earlier than 1000 ns is normalized to unity in these two plots..

needed to assign the hits to the shower corresponding to the originated particle. Therefore, the clustering algorithm affects the input of the time reconstruction algorithm. In this section, to first decouple the impact of the clustering algorithm, we quantify the performance of the algorithm in single-particle events by considering all the hits in each event as a perfect cluster. The reconstructed time is compared with the true shower time, where the true time of a shower is defined as the earliest true projected time of the shower hits.

Fig. 8 shows the distribution of the time difference between the reconstructed value and the true value in the 10 GeV  $\pi^+$  sample. This distribution highly depends on the parameter  $R$ . When  $R$  is too small or

too large, the resulting residual spectrum shows a large width followed by a long tail on one side. On the contrary, when  $R$  is in an optimal region, the residual distribution is relatively narrow and symmetrical.

The bias and resolution of time reconstruction are extracted from the residual distribution to quantify and optimize the algorithm performance. The bias and resolution are defined as the mean and standard deviation of the residual, respectively. The error on the resolution is evaluated by  $\frac{1}{2\sigma} \sqrt{\frac{1}{n} (\mu_4 - \frac{n-3}{n-1} \sigma^4)}$  [19] where  $\mu_4$  and  $\sigma$  are the fourth moment and standard deviation of the residual, and  $n$  denotes the number of hits in the bin. The calculated bias and resolution versus  $R$  are shown in Fig. 9 and 10. Except for muons, the  $R$  minimizing the resolution slightly differs from that for unbiased reconstruction. In more detail,  $R$  can be optimized according to the PID information and energy. The optimal  $R$  of hadronic showers is smaller than the value of the EM shower since the tail of the projected time spectrum of hadronic showers is much more significant than that of photon and muon. Moreover, the muon contains few later hits, so this kind of shower corresponds to an  $R \sim 0.5$ .

The dependence of the bias and resolution on the incident momentum of the particle is shown in Fig. 11. The value of  $R$  is fixed at 0.4. The time resolution of the EM showers with energy higher than 1 GeV is better than 20 ps. As the incident momentum increases, the time resolution improves statistically because of the increasing number of hits in showers. When the momentum increases above 25 GeV, the time resolution reaches less than 5 ps. Because the thickness of the ECAL is only  $26 X_0$ , a fraction of the energy of the hadronic particle can not deposit in ECAL. This fact causes the time resolution of the hadronic showers to be 80 to 150 ps, worse than that of EM showers. In Fig. 11, there appears to be a step around 10 GeV. This step exists in the hadronic particle samples simulated with the physics lists of QGSP\_BERT and QGSP\_BERT\_HP and is waiting for further exploration. Moreover, as minimum ionization particles, muons tend to create about one hit of  $\sim 1$  MIP per layer along their trajectory. Consequently, the time resolution of muons is independent of the incident energy and is nearly 1/5 the intrinsic time resolution of an individual one MIP hit.

## 5 Scaling with changing intrinsic hit time resolution and layers number

The cluster ToF performance strongly depends on the intrinsic time resolution of each individual ECAL chan-

**Fig. 8** The distribution of the difference between reconstructed shower time and the true time in the 10 GeV  $\pi^+$  sample. To remove the outliers, a time residual window (red lines) is defined as  $[Q_2 - 5(Q_3 - Q_1), Q_2 + 5(Q_3 - Q_1)]$ , where  $Q_1$ ,  $Q_2$  and  $Q_3$  are the three quartiles of the distribution. The bias and resolution is defined as the mean and standard deviation of the data inside the window.

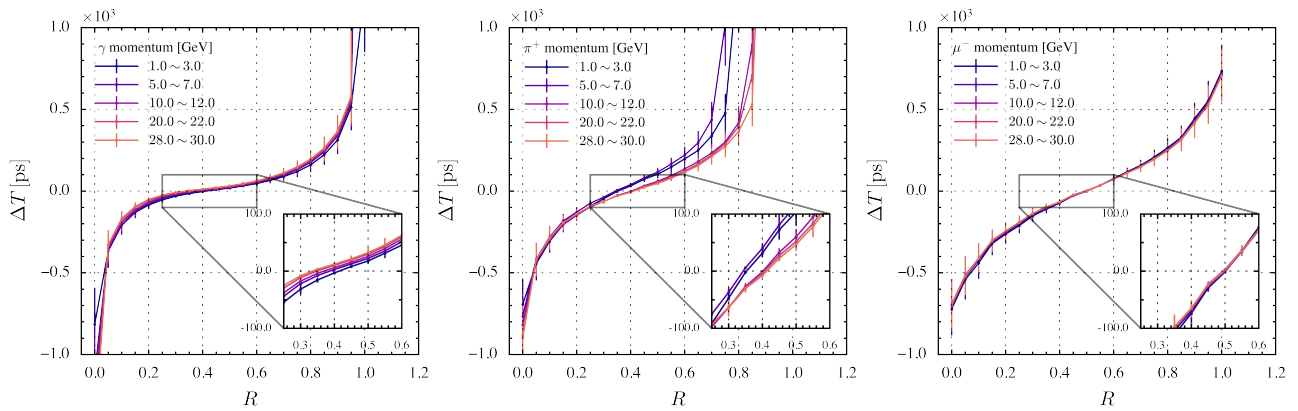
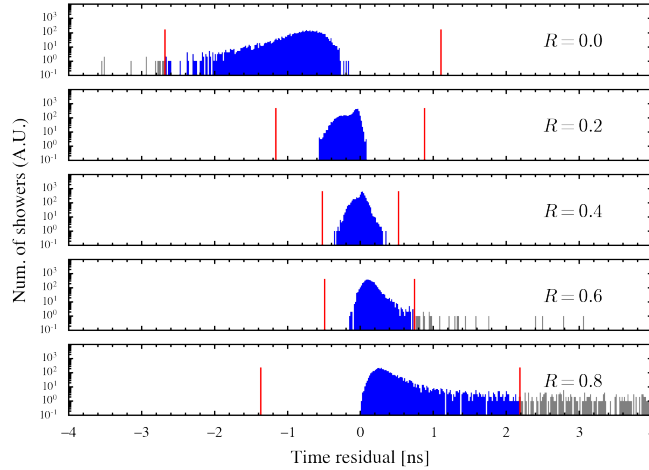


**Fig. 9** Bias of reconstructed shower time in  $\gamma$  (left),  $\pi^+$  (middle),  $\mu^-$  (right) samples as a function of  $R$ . The errors are all scaled with a factor of ten, and also in Fig. 10.

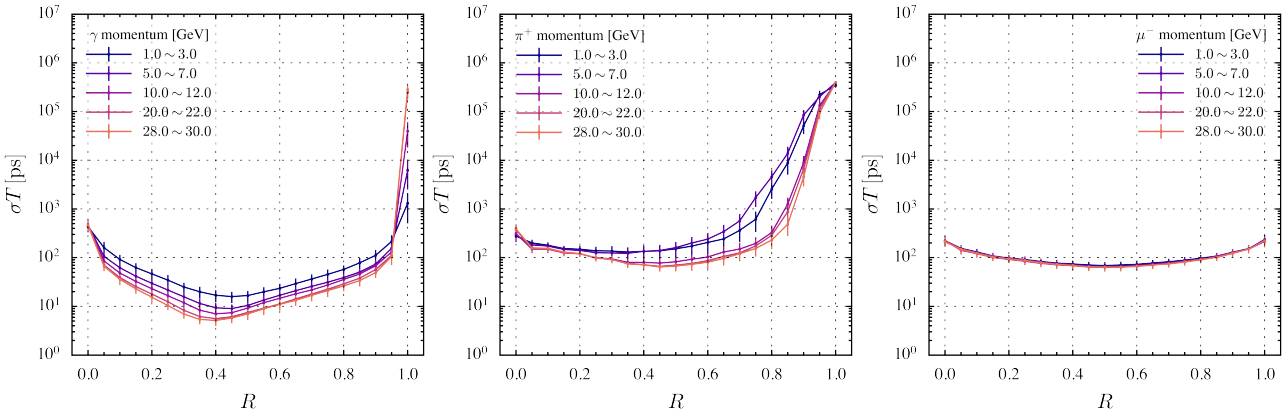


**Fig. 10** The shower time resolution in the  $\gamma$  (left),  $\pi^+$  (middle),  $\mu^-$  (right) samples as a function of  $R$ .

nel. In this section, we quantify the dependence of ToF resolution on the intrinsic hit time resolution by scaling the intrinsic hit time resolution with a factor  $\alpha$ ,

$$\sigma = \alpha \cdot \sqrt{\left(\frac{A}{E}\right)^2 + C^2}, \quad \left( \begin{array}{l} A = 380 \text{ ps} \cdot \text{MIP}, \\ C = 10 \text{ ps} \end{array} \right) \quad (3)$$

and observing the optimal resolution versus different factors. Furthermore, the arrangement of the timing

readout layers also impacts the ToF reconstruction. This arrangement should be optimized to balance the detector performance and building cost. In order to briefly explore the impact of the timing layers arrangement, we only choose a part of the ECAL layers with equal distance, perform the time reconstruction using the hits on these chosen layers, and finally observe the relationship between the ToF resolution and the number of timing

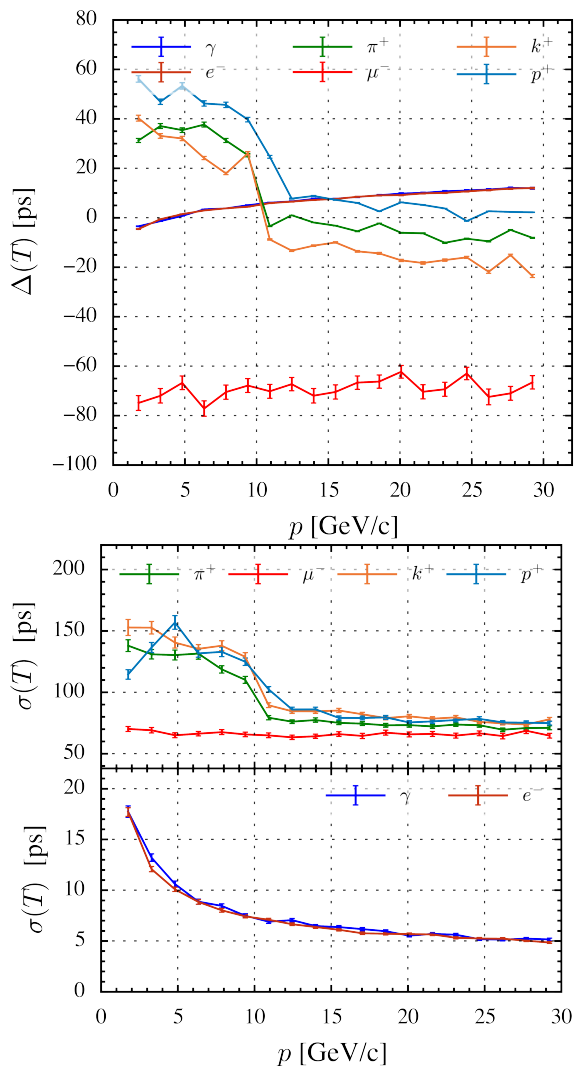


**Fig. 11** With  $R = 0.4$ , the time reconstruction bias (top) and resolution (bottom) of  $e^-$ ,  $\mu^-$ ,  $\pi^+$ ,  $K^+$  and  $p$  as a function of the incident momentum.

layers. In the case of only several timing layers, the impact of the layer position is also discussed.

The ToF resolution versus the scaling factor ( $\alpha$ ) of the intrinsic hit time resolution is shown in Figure 12. When the single hit time resolution is scaled from 100 to 0.1 times the level in Fig. 6, the cluster time resolution reflects an approximately linear relationship with the intrinsic hit time resolution.

The shower time resolution as a function of the number of layers is shown in Fig. 12, where the timing layers are arranged at isometric intervals. The cluster timing performance statistically deteriorates when the number of timing layers decreases since the input hit times of the algorithm become fewer and fewer. Fig. 13 shows the impact of the timing readout arrangement when only one layer provides timing information. EM shower time resolution reaches the highest when the timing

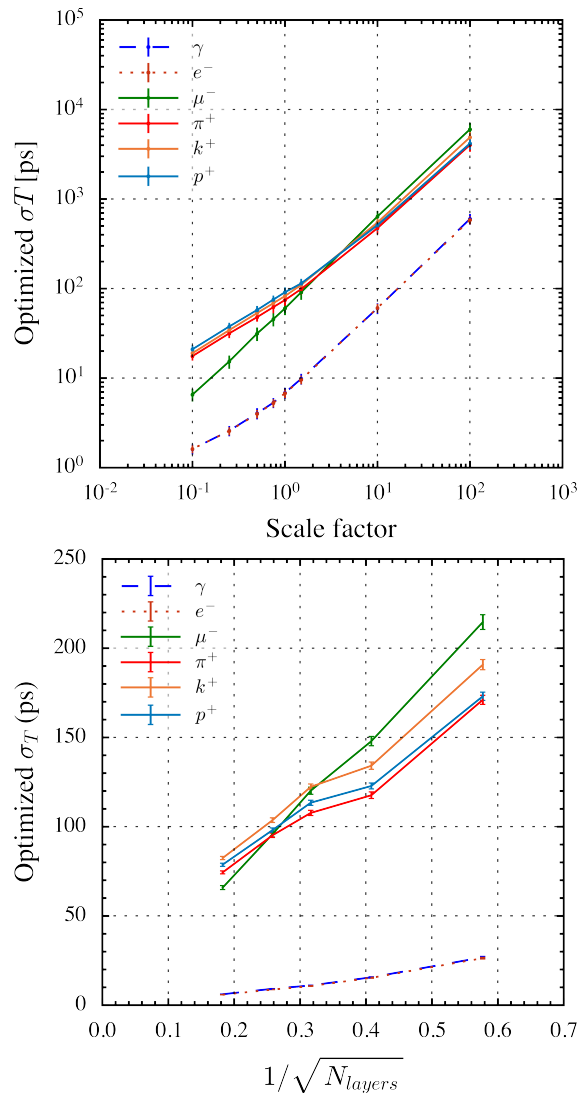


**Fig. 12** The scaling behavior of the shower time resolution for 10 ~ 15 GeV particles versus the intrinsic hit time resolution (top) and the number of timing layers (bottom).  $\alpha$  denotes the scale factor in Eq. 3

readout is located on the 10 ~ 15th layer, where the depth corresponds to  $6 \sim 9 X_0$  and the energy deposition of EM showers is more intense. The optimal time resolution of EM showers is about  $\sim 20$  ps, which is consistent with the test beam result of the CMS HG-CAL timing layer [13, 14]. When the timing readout is installed on the first or last few layers, the reconstruction performance and efficiency decrease, as shown in the second plot of Fig. 13. For hadronic showers, the time resolution improves with the timing layer moving to a deeper position. The effect of timing layers arrangement on the timing of muon is marginal since the energy deposition is highly uniform. Furthermore, considering the better timing performance arising from the layers around the shower maximum, the shower

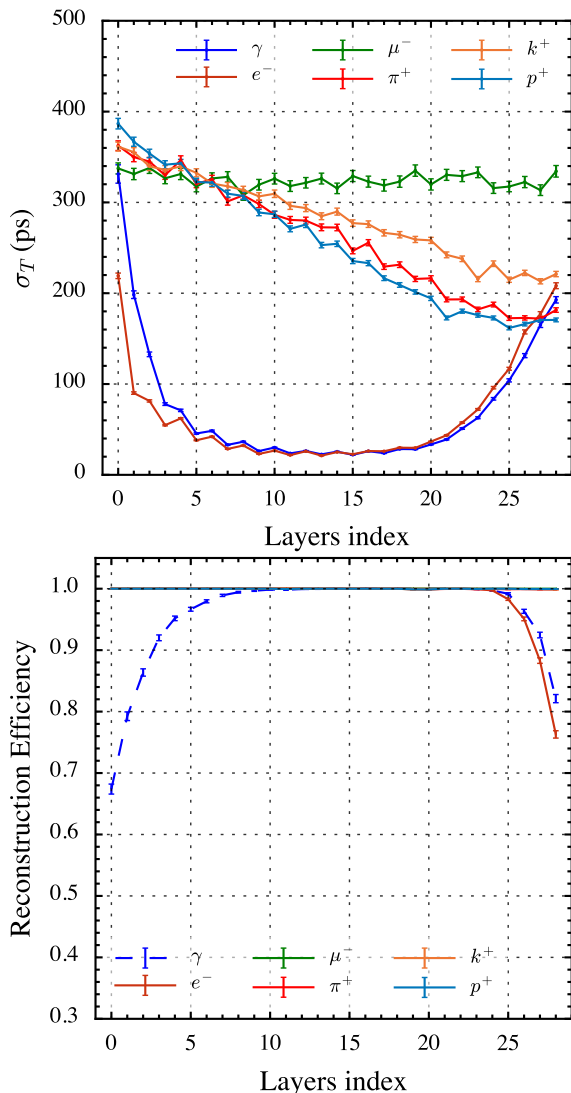


**Fig. 13** The time resolution (top) and corresponding efficiency (bottom) from a single layer for 25 ~ 30 GeV particles as a function of the layer index.

timing performance is hopeful to be improved by installing several dedicated silicon timing layers with high precision, such as the LGAD [7, 20], at the key position. From this perspective, further research and testing about the response of these high-precision timing sensors on calorimeters will be beneficial.

With the above observation, we can briefly estimate the timing precision of the CMS CE-E. The difference in the number of timing layers can only contribute a variance of 7% on shower time resolution. On the other hand, the depletion thickness of silicon sensors is 120  $\mu\text{m}$ , 200  $\mu\text{m}$  and 300  $\mu\text{m}$  in the three parts of CE-E corresponding to different radiation fluence. We assume that the three types of silicon sensors can provide the same time resolution of the sensors with depletion thickness of 133  $\mu\text{m}$ , 211  $\mu\text{m}$  and 285  $\mu\text{m}$  tested in

Ref [1], and the time uncertainty from the distributed clocks of each channel can be well controlled by calibration algorithms. The ToF resolution of photons with  $p_T = 5$  GeV that can be reached in the three parts of CE-E should be approximately 1.8, 1, and 0.9 times the resolution estimated in the CEPC ECAL setup, which is listed in Table 3.

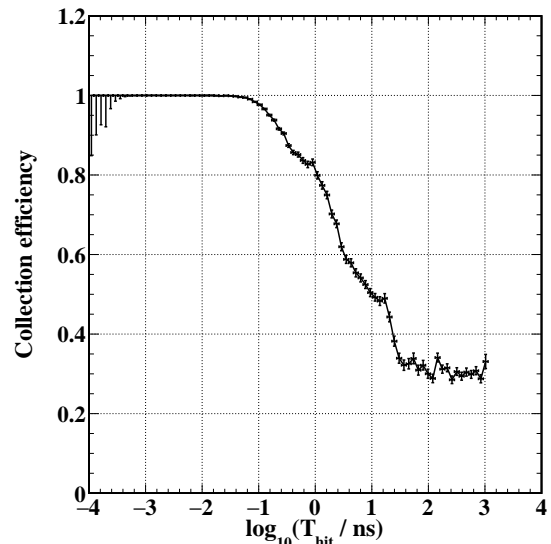


**Fig. 14** The hit collection efficiency of Arbor versus the true time of ECAL hits, calculated in the 10 GeV  $\pi^+$  sample.

## 6 Impact of realistic clustering module

The clustering algorithm is the core part of the PFA, which divides the hits into clusters corresponding to the shower generated by the final states. In the ideal case, all the hits can be collected to the clusters that, one by one, correspond to the incident particles. However, this task is difficult in the real-world scenario with high particle multiplicity. In fact, various algorithms use different strategies to decide how to cluster the hits. For example, the PFA used in the CEPC, Arbor [21], selects hits according to their position and tends to remove the shower hits on the periphery of the shower. Because of the correlation of the hit time and position, Arbor has higher collection efficiency for hits in the fast component than for later hits, as shown in Fig. 14. Consequently, the clustering algorithm impacts the ToF reconstruction.

Fig. 15 compares the time reconstruction bias and resolution for the perfect and Arbor clustering algorithms. Because the later hits are partly removed, the optimal  $R$  for the Arbor clusters is slightly larger than



**Table 3** The depletion thickness of silicon sensors, assumed noise term coefficient of the intrinsic time resolution (which is the same with the beam test result in Ref. [1]), and ToF resolution for photons with transverse momentum of 5 GeV estimated in the setup of CEPC ECAL and the three parts of CE-E along transverse radius.

Radius range (cm)	30 ~ 70	70 ~ 100	100 ~ 180
p ( $p_t = 5\text{GeV}$ )	23 ~ 54	17 ~ 23	10 ~ 17
Shower time resolution on CEPC ECAL (ps)	< 5	~ 6	6 ~ 7
Active thickness ( $\mu\text{m}$ )	120	200	300
Noise term A (ns · MIP)	0.69	0.38	0.34
Variance factor of $\sigma(t)$ contributed by intrinsic $\sigma(t)$	1.8	1	0.9
Variance factor of $\sigma(t)$ contributed by $N_{layers}$	1.07	1.07	1.07
Shower time resolution on CMS CE-E (ps)	< 10	~ 6	6

**Fig. 15** The shower time resolution as a function of  $R$  value for perfect clusters and Arbor clusters in the photon (left) sample and the pion (right) samples. The error bars are multiplied by a factor of five for visibility.

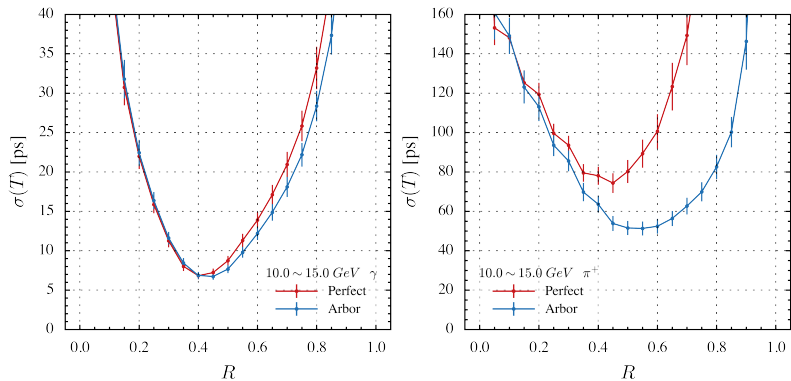
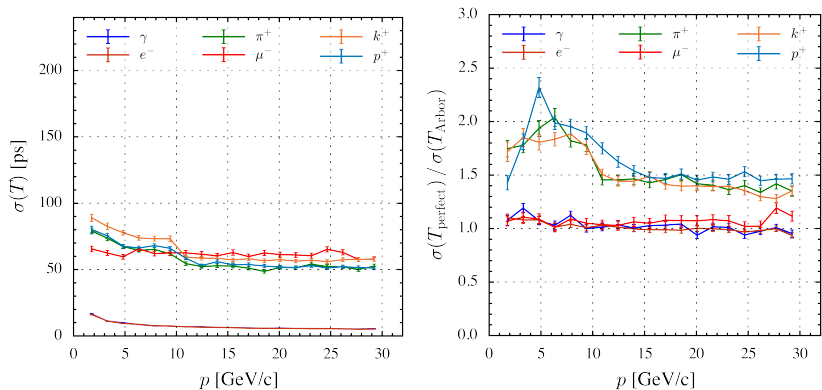


**Fig. 16** The shower time resolution for the Arbor clusters (left) and the time resolution ratio of perfect clusters over Arbor clusters (right) as a function of incident momentum.



that of the perfect clusters. Fig. 16 shows the ToF resolution of the Arbor clusters and its ratio over the resolution for the perfect clusters.  $R$  is fixed at 0.45 for Arbor clusters and 0.4 for perfect clusters in this figure. Arbor can improve the time resolution of 50 ~ 90% for hadronic clusters, while the improvement for the EM clusters is up to 10%. In addition, the improvement of the hadronic showers is more significant when the incident momentum is lower than 10 GeV. The step in Fig. 11 disappears in the first plot of Fig. 16, which implies that the step in Fig. 11 may arise from the hits on the periphery of the shower.

## 7 Summary

We propose a quantile-based time reconstruction algorithm that extracts the ToF of particles from shower hits in HGC with typical density of  $\mathcal{O}(1 \sim 10)$  channels per cubic centimeter. The hit time is subtracted by the time it takes for the light to travel from the IP to the hit position. This algorithm chooses the quantile of the hit times as the reconstructed shower time. The time resolution of each channel is parameterized to be  $\frac{0.38 \text{ ns} \cdot \text{MIP}}{E} \oplus 10 \text{ ps}$  according to the test of the CMS silicon sensor in Ref. [1]. We expect that a time resolution of 5 to 20 ps (80 to 160 ps) can be achieved for EM (hadronic) showers on the CEPC ECAL.

The presented algorithm and several alternative strategies based on the average of the hit times with energy

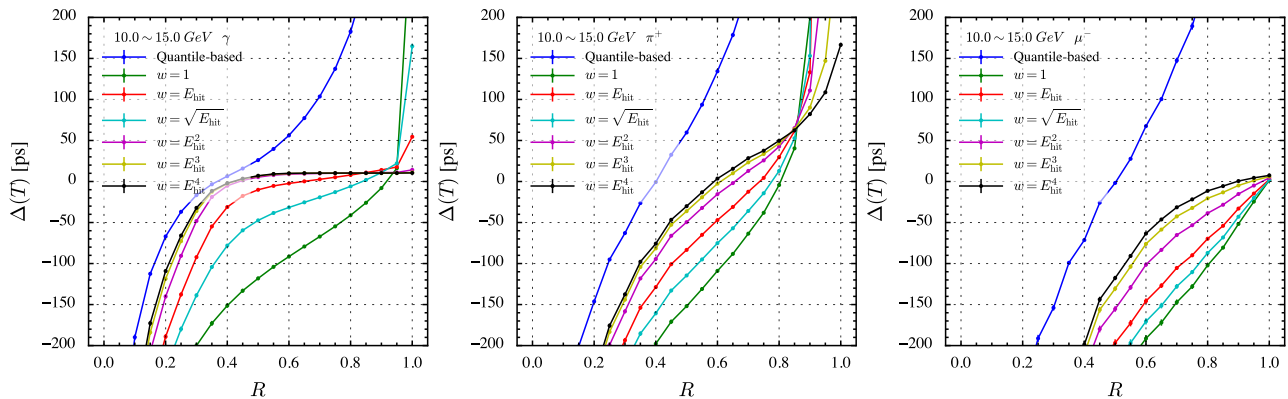


**Fig. 17** The shower time reconstruction bias from quantile-based algorithm and average-based algorithms with energy weights of  $E_{\text{hit}}^n$ ,  $n = 0, 1/2, 1, 2, 3, 4$  as a function of  $R$ .

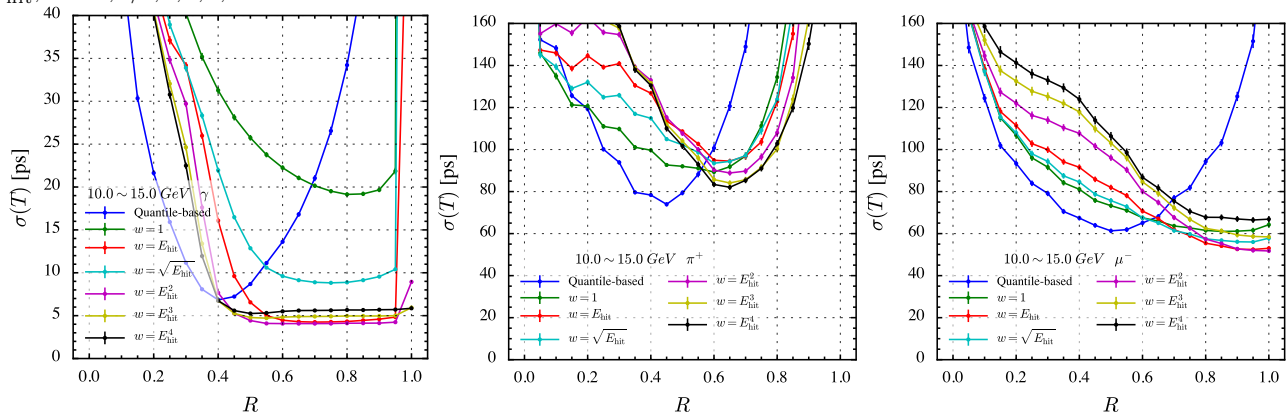


**Fig. 18** The shower timing bias(top) and resolution(bottom) from quantile-based algorithm and average-based algorithms with energy weights of  $E_{\text{hit}}^n$ ,  $n = 0, 1/2, 1, 2, 3, 4$  as a function of  $R$ .

weighting are compared. The average with  $E^2$  weighting can improve the time resolution of EM (hadronic) showers from 20 ps (90 ps) to 4 ps (85 ps), comparable with the quantile-based algorithm.

We investigate three relevant factors for the ToF measurement, the intrinsic hit time resolution, the number of layers, and the time clustering algorithm. First, we observe an approximately linear dependence between the cluster ToF resolution and the intrinsic time resolution of each channel. Second, the time resolution of the showers statistically improves with the number of calorimeter timing layers if these timing readouts are uniformly installed in the ECAL. When the number of timing layers is small, optimizing the layout of timing layers is favorable. The time resolution of EM showers can be significantly improved by installing the layer in  $6 \sim 9X_0$ , while the last ten layers are more advantageous for timing hadronic showers. Thirdly, a specific clustering algorithm affects the timing performance because the hit time is correlated with the hit position. For example, Arbor leads to an improvement of up to  $< 10\%$  ( $40 \sim 90\%$ ) for EM (hadronic) showers, compared to an ideal clustering module.

With the understanding above, we evaluate the timing performance of the electromagnetic compartment of the CMS endcap calorimeter. If the intrinsic time resolution of each channel is similar to the result of Ref. [1], we expect that this calorimeter can provide 6 to 10 ns time resolution for photons with a transverse momentum of 5 GeV. This precision is beneficial for pile-up mitigation.

In this work, the distributed clock is assumed to be well synchronized by hardware technology and calibration algorithms. The current silicon sensors have high precision timing capability for hits with energy of hundreds MIPs but relatively low time resolution for those with only several MIPs. In addition, there are still many interesting patterns in the true time-energy spectrum of the showers. As HGC timing performance improves to picosecond level, these patterns will increasingly affect relative measurements. Therefore, it is valuable to model the timing information of the showers with high precision in Monte Carlo simulations and analyse the patterns at the picosecond level.

**Acknowledgements** The authors thank Jianbei Liu, Yong Liu, Huaqiao ZHANG and Jean-Claude Brient for their help in interpreting the timing readout technique. We also thank Chengdong FU and Dan YU for their assistance with the simulation software, and Xuewei JIA for fruitful discussions and language support in this work. This project is supported by the International Partnership Program of Chinese Academy of Sciences (Grant No. 113111KYSB20190030), the Innovative Scientific Program of Institute of High Energy Physics.

## Appendix A: Average based strategy

This section compares the proposed time reconstruction algorithm with several alternative average-based strategies that average over the hit times with different energy weights after removing a part of the shower hit relatively later in the time spectrum.

The average-based algorithms first sort the recorded hits in ascending order according to the hit time. Secondly, the energy-weighted average time of the first ( $R' \cdot N_{hits}$ ) hits is calculated as the result.  $R'$  is also an ad hoc ratio similar to  $R$  in the quantile-based algorithm. The quantile-based algorithm essentially removes a part of the latest hits in the shower, where the fraction of removed hits is  $2R$ . Then the  $R \cdot N_{hits}$ -th hit time is equivalent to the median of the remaining hit times. In this study, five hit energy weighting models,  $E_{hit}^n$  ( $n = 0, 1/2, 1, 2, 3$ ), are considered.

The quantification in Sec. 4 is applied to the average-based algorithm in photon, charged pion, and muon samples. As shown in Fig. 18, the performance of the average-based strategy can be significantly improved by energy weighting. The time resolution of EM showers from  $E^2$  weighted average strategy reaches  $\sim 4$  ps,  $\sim 5$  times better than the result of the unweighted average strategy and higher than the quantile-based algorithm by  $\sim 2$  ps. For the hadronic showers and MIP, the impact of energy weighting on the time resolution is relatively small.

## References

1. N. Akchurin, V. Ciriolo, E. Currás, J. Damgov, M. Fernández, C. Gallrapp, L. Gray, A. Junkes, M. Mannelli, K.M. Kwok, et al., Nuclear Instruments and Methods in Physics Research Section A: Accelerators, Spectrometers, Detectors and Associated Equipment **859**, 31 (2017)
2. G. Apollinari, I. Béjar Alonso, O. Brüning, P. Fesia, M. Lamont, L. Rossi, L. Tavian, High-luminosity large hadron collider (hl-lhc). technical design report v. 0.1. Tech. rep., Fermi National Accelerator Lab.(FNAL), Batavia, IL (United States) (2017)
3. A. Bornheim, D. Anderson, C. Pena, A. Apresyan, M. Spiropulu, J. Duarte, S. Xie, A. Ronzhin, in *XIII Pisa Meeting on Advanced Detectors* (2015)
4. CMS collaboration, CERN-LHCC-2017-027. LHCC-P-009 (2017)
5. CMS Collaboration, The phase-2 upgrade of the cms endcap calorimeter cern-lhcc-2017-023. Tech. rep., CMS-TDR-019 (2017)
6. O. Cerri, arXiv preprint arXiv:1810.00860 (2018)
7. ATLAS collaboration, CERN, Geneva, Tech. Rep., Jun (2020)
8. European Strategy Group Collaboration. 2020 update of the european strategy for particle physics (2020)
9. F. An, S. Prell, C. Chen, J. Cochran, X. Lou, M. Ruan, The European Physical Journal C **78**(6), 1 (2018)
10. Y. Guz, JINST **15**(09), C09046 (2020). DOI 10.1088/1748-0221/15/09/C09046
11. V. Boudry, PoS **ICHEP2020**, 823 (2021). DOI 10.22323/1.390.0823
12. F. Cavallari, JINST **15**(03), C03041 (2020). DOI 10.1088/1748-0221/15/03/C03041
13. A. Apresyan, in *2016 IEEE Nuclear Science Symposium, Medical Imaging Conference and Room-Temperature Semiconductor Detector Workshop (NSS/MIC/RTSD)* (IEEE, 2016), pp. 1–8
14. A. Apresyan, G. Bolla, A. Bornheim, H. Kim, S. Los, C. Pena, E. Ramberg, A. Ronzhin, M. Spiropulu, S. Xie, Nuclear Instruments and Methods in Physics Research Section A: Accelerators, Spectrometers, Detectors and Associated Equipment **825**, 62 (2016)
15. N. Akchurin, A. Apreysan, S. Banerjee, D. Barney, B. Bilki, A. Bornheim, J. Bueghly, S. Callier, V. Candelise, Y.H. Chang, et al., Journal of Instrumentation **13**(10), P10023 (2018)
16. CEPC Study Group, arXiv preprint arXiv:1811.10545 (2018)
17. C. Lange, PoS **EPS-HEP2021**, 846 (2022). DOI 10.22323/1.398.0846
18. S. Agostinelli, J. Allison, K.a. Amako, J. Apostolakis, H. Araujo, P. Arce, M. Asai, D. Axen, S. Banerjee, G. Barrand, et al., Nuclear instruments and methods in physics research section A: Accelerators, Spectrometers, Detectors and Associated Equipment **506**(3), 250 (2003)
19. C.R. Rao, *Linear statistical inference and its applications*, 2nd edn. Wiley series in probability and statistics (Wiley)
20. H.F. Sadrozinski, A. Seiden, N. Cartiglia, Reports on Progress in Physics **81**(2), 026101 (2017)
21. M. Ruan, arXiv preprint arXiv:1403.4784 (2014)